

A Machine Learning Framework for Drill-Core Mineral Mapping Using Hyperspectral and High-Resolution Mineralogical Data Fusion

Isabel Cecilia Contreras Acosta , Mahdi Khodadadzadeh , Laura Tusa,
Pedram Ghamisi , Senior Member, IEEE, and Richard Gloaguen

Abstract—Mining companies heavily rely on drill-core samples during exploration campaigns as they provide valuable geological information to target important ore accumulations. Traditional core logging techniques are time-consuming and subjective. Hyperspectral (HS) imaging, an emerging technique in the mining industry, is used to complement the analysis by rapidly characterizing large amounts of drill-cores in a nondestructive and noninvasive manner. As the accurate analysis of drill-core HS data is becoming more and more important, we explore the use of machine learning techniques to improve speed and accuracy, and help to discover underlying relations within large datasets. The use of supervised techniques for drill-core HS data represents a challenge since quantitative reference data is frequently not available. Hence, we propose an innovative procedure to fuse high-resolution mineralogical analysis and HS data. We use an automatic high-resolution mineralogical imaging system (i.e., scanning electron microscopy–mineral liberation analysis) for generating training labels. We then resample the MLA image to the resolution of the HS data and adopt a soft labeling strategy for mineral mapping. We define the labels for the classes as mixtures of geological interest and use the classifiers (random forest and support vector machines) to map the entire drill-core. We validate our framework qualitatively and quantitatively. Thus, we demonstrate the ability of the proposed technique to fuse and up-scale high-resolution mineralogical analysis with drill-core HS data.

Index Terms—Data fusion, drill-cores, hyperspectral (HS) data, machine learning, mineral liberation analysis (MLA), random forest (RF), support vector machine (SVM).

I. INTRODUCTION

D RILL cores are cylindrical rock samples, which are commonly extracted in exploration campaigns by drilling holes into the Earth's subsurface up to a few kilometers. Drill-cores are a few centimeters in diameter, wide enough to allow exploring the geology of the underlying bedrock ore environment [1]. When the number of drill-cores is high, they allow

Manuscript received January 24, 2019; revised May 16, 2019; accepted June 11, 2019. Date of publication July 8, 2019; date of current version February 4, 2020. (Corresponding author: Isabel Cecilia Contreras Acosta.)

The authors are with the Division of "Exploration Technology", Helmholtz-Zentrum Dresden-Rossendorf, Helmholtz Institute Freiberg for Resource Technology, Freiberg, 09599 Germany (e-mail: i.contreras@hzdr.de; m.khodadadzadeh@hzdr.de; l.tusa@hzdr.de; p.ghamisi@hzdr.de; r.gloaguen@hzdr.de).

Color versions of one or more of the figures in this paper are available online at <http://ieeexplore.ieee.org>.

Digital Object Identifier 10.1109/JSTARS.2019.2924292

to statistically represent the entire geological deposit. Fig. 1(a) shows a simplified sketch of a geological ore deposit, where the red lines represent examples of drill holes. Once drill-cores are extracted, they are organized in so-called drill-core trays [see Fig. 1(b)].

Drill-cores are analyzed by experts following core logging techniques. Core logging is a systematic approach that assimilates a wide range of data obtained from the cores to determine the lithology, structures, and alteration zones of a potential mineral deposit [1]. Exploration and mining companies strictly rely on the mineralization information obtained by core logging techniques (e.g., the mineral assemblages, alteration patterns, and structural features) to target important ore accumulations and obtain a preliminary information about the composition and size of an ore deposit.

The drilling phase is commonly the most expensive part of the mineral exploration campaigns. Thus, extracting as much mineralogical information as possible from the cores is crucial. Traditionally, laboratory techniques such as optical microscopy [2], X-ray diffraction (XRD) [3], and X-ray Fluorescence (XRF) [4] are also used to characterize small selected drill-core samples. Moreover, high-resolution mineralogical analyses have recently been adopted to support geologists in the identification and quantitative evaluation of minerals. For such analyses, scanning electron microscopy (SEM) data integrated with the mineral liberation analysis (MLA) [5] or with the QEMSCAN [6] software are applied on selected polished thin sections of drill-cores in the laboratory. Although these techniques provide important and relevant mineralization information, they are extremely time-consuming taking up to six hours for the analysis of one thin section. In addition, they are costly and the commercial turnaround can be lengthy. This represents an issue since hundreds of meters of cores are extracted during exploration campaigns.

Hyperspectral (HS) imaging is an emerging technique in the mining industry that enables a noninvasive and nondestructive characterization of large amounts of drill-cores in a fast turnaround time [7]–[11]. HS data are recorded in several tens of spectral bands, which allows constructing rich reflectance spectrum profiles. Such profiles can be used for the task of mineral mapping, which aims at determining the spatial distribution of minerals in drill-cores. Minerals have varied spectral responses in the visible and infrared part of the electromagnetic spectrum.

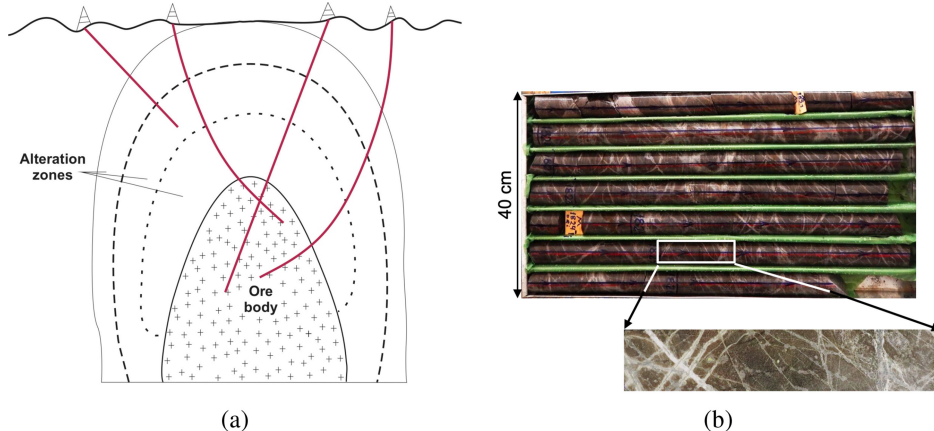


Fig. 1. (a) Sketch of an alteration system. Different alteration zones surround the ore body located in the center of the system. Drill holes are represented by the red lines. (b) Example of a drill-core tray and a drill-core sample. The length of the drill-cores in the tray tends to be 1 m.

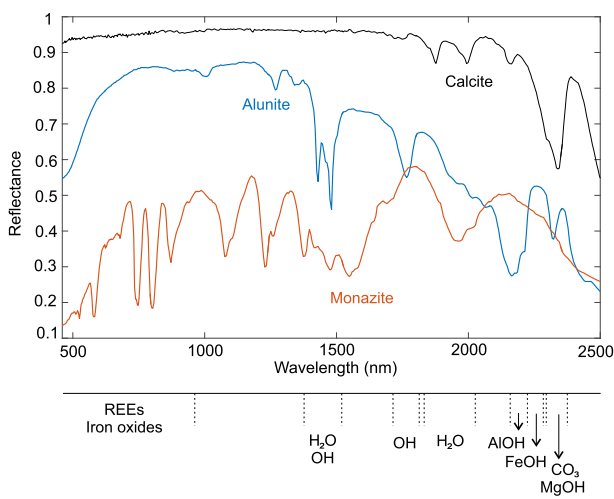


Fig. 2. Major spectral absorption bands in the VNIR-SWIR. Sample spectra from the USGS [14].

These responses are triggered by the vibrational and electronic absorption processes, which depend on the bonds between their atoms and their electron orbitals [12], [13]. Also, mineral assemblages and grain size have an effect on the spectral responses. Fig. 2 shows the major absorption regions in the visible and near-infrared (VNIR) and short-wave infrared (SWIR) parts of the electromagnetic spectrum and their associated molecular bonds. Moreover, Table I summarizes the responses of some important minerals in the VNIR, SWIR, and long-wave infrared (LWIR).

The accurate analysis of drill-core HS data is becoming more and more important. Commonly, a reference spectral library (e.g., United States Geological Survey (USGS) Spectral Library [15]) is used to identify and map adequate minerals. A geologist visually compares the absorption features and general shape of the samples spectra in the data with the spectra from the library [16], [17]. Another common approach, due to its simplicity and availability, is based on the following steps: 1) dimensionality reduction using a minimum noise fraction transformation [18], [19]; 2) selection of representative samples or end-members, using the pixel purity index (PPI) and the n-Dimensional (n-D)

TABLE I
SUMMARY OF INFRARED ACTIVE MINERALS

Mineral group	VNIR	SWIR	LWIR
Phyllosilicates	nonactive	good	moderate
Mica, Clay, Chlorite			
Hydroxylated silicates	nonactive	good	moderate
Epidote, Amphiboles			
Anhydrous silicate	nonactive	nonactive	good
Quartz, Feldspar group	nonactive		
Sulfates	nonactive	good	moderate
Alunite, Gypsum			
Carbonates	nonactive	moderate	good
Calcite, Dolomite, Ankerite			
Oxides	good	nonactive	nonactive
Hematite, Magnetite			

Visualizer [20]; 3) manual or automatic identification of the end-members using spectral libraries and the spectral analyst; 4) mineral mapping and/or determination of partial abundances using spectral similarity measure algorithms [e.g., spectral angle mapper (SAM)], spectral feature fitting [7], [8], [21], or unmixing algorithms (e.g.; linear unmixing, mixture tune matched filtering) [22], [23]. This chain of techniques has been implemented in the Environment for Visualizing Images (ENVI, Exelis Visual Information Solutions, Boulder, CO, USA) software. Moreover, only a few automatic techniques based on exploiting specific absorption features, such as wavelength position, depth, and width of the features, have been proposed to exclusively map specific minerals [24]–[26]. Although the aforementioned approaches have shown good results, they require a large amount of expert interaction, thus, can be subjective and time-consuming.

Recently, to improve the speed and accuracy of data analysis, the use of machine learning classification techniques has been suggested in different scientific fields. Given a limited number of known observations (i.e., training data), the goal of a classification system is to learn the characteristics of a set of predefined classes and assign a unique class label to each unknown data sample. Machine learning classification techniques offer automatic approaches to discover underlying relations

within a large data set. The application of these methods in the geological remote sensing community is growing [27]–[29]. Nonetheless, the implementation of these techniques for the analysis of drill-core HS data has not been fully exploited in the literature. Moreover, defining meaningful classes and selecting representative samples for training a classifier is not straightforward in geological samples. Therefore, the development of innovative solutions is needed.

In this paper, we propose a new framework to use machine learning classification techniques for drill-core HS data analysis. We exploit a data fusion strategy to address the lack of available training samples for the classification. More specifically, we propose to use an automatic high-resolution mineralogical imaging system (i.e., SEM-MLA) for generating training labels to classify HS data. With the help of SEM-based analysis, we first capture a very high-resolution image of a representative but small area of a drill-core sample, which is coded by mineral species. Then, we resample this image to the resolution of the HS data and carefully coregister them. Finally, we exploit the detailed mineralogical information in the resampled MLA image to generate the training set. This integration allows us to make use of the complementary information of both imaging sensors for training a supervised classification system. There have been few attempts in the literature to combine high resolution mineralogical data with HS data [30]–[34]. However, to the best of our knowledge, this combination was mostly being considered to interpret and validate HS data analyses. In this paper, we systematically investigate the fusion of these two sources of information for the first time in the scientific community and use it in an automatic classification framework to up-scale the high-resolution mineralogical information to the entire drill-core data. Once the training is performed and the classifier model parameters are estimated, it can be used to classify a large amount of data automatically. This needs a minimum human interaction and the results are not impacted by the diverse interpretation of different specialists as it happens in traditional visual analysis-based techniques. Another important contribution of this work consists in presenting a flexible labeling strategy for mineral mapping. In our proposed technique, we use SEM-MLA not only for assigning labels to HS drill-core images but also for defining different mineral assemblages corresponding to each class label. In other words, we define our class labels as mixtures of different minerals and use a machine learning classification technique to map these mixtures to the entire drill-core collection. This strategy is aligned with the nature of drill-core HS images where it can be difficult to find pure mineral spectra at a given spatial resolution of the data.

For the classification, we suggest to use RF and SVM since they can handle high-dimensional data with a limited number of training samples [35]–[38]. This is the case in drill-core samples when usually detailed *a priori* information, such as MLA reference maps, is only available for a small area of the drill-core. Moreover, these classifiers are now commonly available in open-source software. Additionally, two well-known endmember extraction algorithms (i.e., the chain of PPI and n-D Visualizer [39] and vertex component analysis (VCA, [40])) are examined in combination with SAM to illustrate results that can be produced by commonly used and available tools.



Fig. 3. SisuRock drill-core scanner equipped with an AisaFenix VNIR-SWIR HS sensor.

TABLE II
USED SENSOR SPECIFICATIONS OF THE SPECIM AISAFENIX
VNIR-SWIR HS CAMERA

Spectral range	380 - 970 nm VNIR 970 - 2500 nm SWIR
Spectral resolution	3.5 nm VNIR 12 nm SWIR
Number of bands	450
Pixel size	1.5 mm/pixels
Spectral binning	4 VNIR 1 SWIR
Scanning speed	25.06 mm/s
Integration time	15 ms VNIR 4 ms SWIR
Frame rate	15 Hz
Field of view	32.3°

The rest of the paper is structured as follows. Section II describes data acquisition (i.e., both HS and high-resolution mineralogy). Section III presents the architecture of the system describing the proposed resampling method and its details. Section IV shows the experimental results, Section V the discussion, and finally, Section VI concludes this paper.

II. DATA ACQUISITION

HS and high-resolution mineralogical data were acquired to show-case the proposed method. Details are presented in the following subsections.

A. Hyperspectral Data

The HS data used in this work were acquired from unpolished halves of drill-core samples with a Specim SisuRock scanner available at the Spectroscopy laboratory at the Helmholtz Institute Freiberg for Resource Technology (see Fig. 3). The scanner is a fully automatic HS imaging workstation, which scans drill-cores in a fast manner. A tray table carries the trays under the field-of-view of the spectrometer. For this study, the SisuRock was equipped with a Specim AisaFENIX HS camera. This camera implements two sensors to cover the VNIR and SWIR regions of the electromagnetic spectrum. Table II shows the sensor specifications used in this study.



Fig. 4. SEM-MLA instrument.

To convert the HS data from radiance values to reflectance, radiometric corrections were performed. For this task, the dark current and white reference measurements were automatically used with a plugin in the acquisition software provided along with the HS camera. To correct the sensor-specific optical distortions (i.e., fish-eye and slit-bending effects on the images) and the spatial shift between the VNIR and SWIR sensors, the toolbox presented in [41] was used.

To avoid bands with little or no coherent information, the data were spectrally subsetted from 380 to 538 nm and from 2486 to 2500 nm by removing the first 47 and the last 3 bands, respectively. The resultant wavelength range covers from 538 to 2486 nm in 400 bands. A smoothing polynomial filter (i.e., Savitzky–Golay filter) was applied to decrease noise while preserving spectral features [42]. Special care was taken to avoid attenuating spectral features while sufficiently smoothing the data. Hence, different settings were tested to finally utilize a filter width of five spectral bands and a third-degree smoothing polynomial.

B. High-Resolution Mineralogical Data

High-resolution mineralogical data of carbon-coated polished thin sections of about $30 \mu\text{m}$ thickness from the drill-core samples were acquired. It was carried out using scanning electron microscope (SEM)-based mineral liberation analysis (MLA) techniques at the Geometallurgy laboratory at the Helmholtz Institute Freiberg for Resource Technology. For this, an FEI Quanta 650 F field emission SEM instrument, equipped with two Bruker Quantax X-Flash 5030 energy dispersive X-ray detectors and the MLA 3.1.4 software suite were used (see Fig. 4) [43]. Note that during the preparation of the carbon-coated thin sections, the surface of the samples was grounded and polished. This led to the removal of about $300 \mu\text{m}$ of material between the rock surface scanned with the HS sensor and the surface studied with the high-resolution mineralogical analysis. Based on the morphology of the samples used for this study and the orientation of structural features, the mineralogical variation is considered negligible with such a small surface shift. However,

in samples where veins are not vertical with respect to the surface or coatings are presented in the surface, the removal of material could influence on the link between the HS and the high-resolution mineralogical data. Thus, special care needs to be taken when preparing and analyzing such samples.

SEM-MLA automates microscope operations and data acquisition for high-resolution mineralogy. The process is summarized in Fig. 5. The SEM generates a beam of electrons that scans the polished thin section. Then, the backscattered electrons (BSE) interact with the minerals and are collected to produce an image, known as the BSE image. Therefore, the BSE image shows the relation between the BSE and the incident electrons coming from the SEM. This relation is represented with different grayscale-levels which are a function of the average atomic number of the minerals [44], [45]. The MLA software collects the BSE images and uses them to effectively segment the mineral grains by distinguishing the boundaries based on the grayscale variations. The grayscale values are used to apply the image segmentation to setup a grid of a given step size that will allow for each grain to be measured. The identification of minerals is performed by collecting the X-ray data on the points of the grid. When the electrons interact with the atoms, X-rays characteristic of specific elements are generated. Finally, the mineral is determined by matching the resultant spectrum of energy peaks with a reference library of X-ray spectra. Specifications of the operating conditions used in this study are shown in Table III, more information on the measurement mode is available in [46], [47].

III. PROPOSED SYSTEM ARCHITECTURE

Fig. 6 shows the proposed machine learning-based system for the analysis of drill-core samples where both HS and high-resolution mineralogical data are fused and used to map minerals and alteration patterns. Following the acquisition of the data, described in Section II, our proposed system can be divided in two main steps:

A. Resampling and Coregistration

To be able to fuse the SEM-MLA and HS data, MLA images need to be resampled with respect to the spatial resolution of the HS image. For this purpose, the most dominant mineral in the MLA image is considered for each resampled pixel (resampled to the HS pixel size). However, in the SEM-MLA analysis, nonactive and active minerals in the VNIR-SWIR part of the electromagnetic spectrum are detectable. More specifically, from the 22 detected mineral groups in the SEM-MLA analysis only ten have specific absorption features in the VNIR-SWIR. Moreover, some minerals are not dominant but are required to be mapped. To account for all these and estimate the mapping of VNIR-SWIR nonactive phases, we adopt a soft labeling strategy in which in all the pixels with the same dominant mineral (considering all the 22 SEM-MLA detected minerals), we count the abundance of all the minerals in these pixels and normalized the values with respect to the entire MLA image. This process is performed in every pixel of the resampled MLA image. In this way,

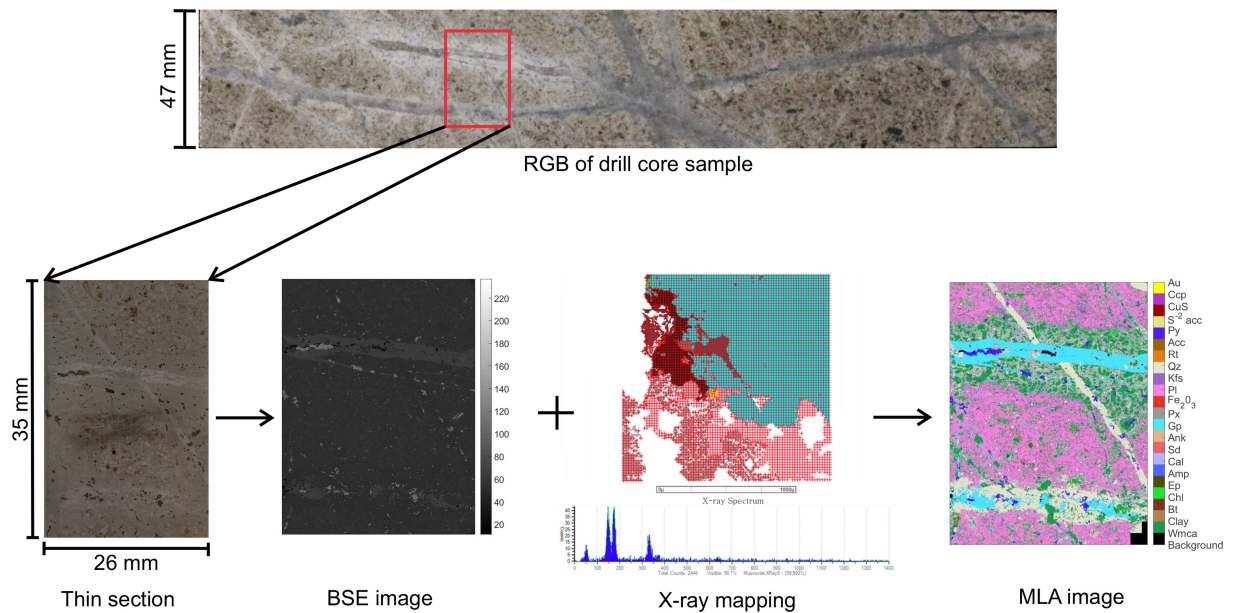


Fig. 5. Summary of the process for the acquisition of SEM data with the MLA software.

TABLE III
USED OPERATING CONDITIONS OF THE SEM-MLA

SEM settings		MLA settings	
Mode	GXM A P	Resolution	1000× 1000 pixels
Frame width	1500 μm	Pixel size	3 μm
BSE calibration	Au 254	Step size	6× 6 pixels
Acceleration voltage	25 kV	Acquisition time	5 ms
Probe current	10 nA	Min. grain size	3 pixels

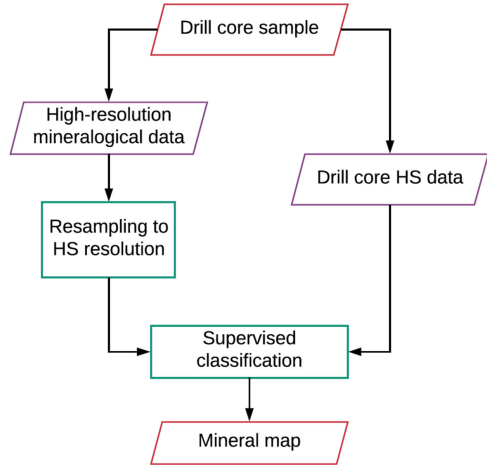


Fig. 6. Flowchart of the proposed machine learning technique to fuse HS and high-resolution mineralogical data for mapping minerals in drill-core samples.

we consider degrees of membership for all the minerals in each class being the percentages associated with the abundance of the classes in the entire MLA image. Thus, the derived abundances provide the means to analyze the different mineral assemblages which then aid with the interpretation of the spectral variations amongst classes and the mineral distributions.

To illustrate the resampling process better, Fig. 7 shows an example of the proposed method. From the simplified MLA image shown in Fig. 7(a), the dominant mineral in each HS pixel size (represented by the grid on top) is considered for the MLA resampled image. Hence, one class based on the dominant mineral has been assigned to each pixel in the MLA resampled image [see Fig. 7(b)]. In the case of the upper-left and lower-right pixels, both have muscovite as the dominant minerals, therefore, both are assigned to class 1. For the upper-right and lower-left pixels, chlorite and gypsum are the dominant minerals, respectively. Therefore, class 2 and class 3 are assigned to these pixels. From the soft labeling strategy, we obtain the degree of membership or mineral abundances associated with each class [see Fig. 7(c)]. For this, the abundances of the minerals for each class are obtained by normalizing the percentages of all the minerals in all the pixels corresponding to the same class with respect to the entire MLA image. For example in Fig. 7(c), the abundances of the minerals for class 1 are obtained by normalizing the percentages of each mineral for both pixels assigned with class 1 (upper-left and lower-right pixels). Finally, Fig. 7(d) shows the spectrum corresponding to the pixel in the upper-right corner which corresponds to class 2 (mainly composed by chlorite).

After the MLA images are resampled, they need to be coregistered with the HS images. For this, the MLA resampled images are carefully compared by visually setting tie points on their respective HS images. This is supported by the analysis of structural features found on the surface of the drill-core samples, mineral composition, and spectral responses.

B. Classification

The last step in our proposed framework consists in extending the extracted information from the SEM-MLA high-resolution mineralogical data to the entire drill-core data by predicting the labels of each pixel in the drill-core HS image. HS features

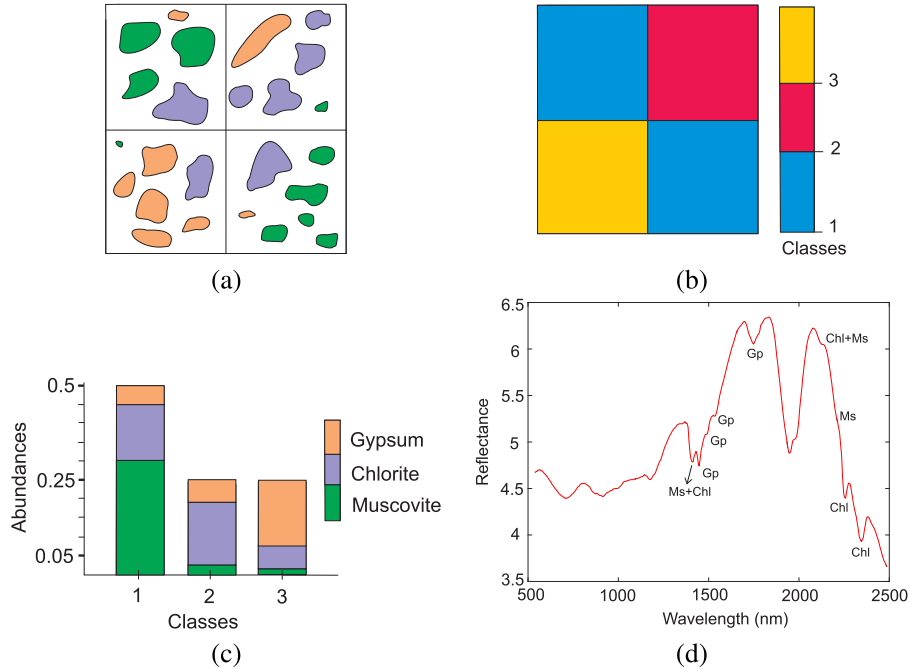


Fig. 7. Summary of the proposed resampling process: (a) Sketch of an MLA image with a grid indicating the HS pixels. For each pixel, the most dominant mineral in the MLA image is used to define the MLA resample map shown in (b). (c) Abundances associated with each of the resultant classes obtained by the proposed soft labeling strategy. (d) Spectrum of class 2, corresponding to the pixel in the upper-right corner, with the specific absorption features of each mineral in the mixture. Mineral abbreviations after [48].

together with the MLA reference map are used as input for a supervised classifier. Two well-known machine learning classifiers which have been demonstrated having good performance in geological applications are employed.

1) *Random Forest (RF)*: RF is an ensemble learning classifier, in which a set of decision tree (DT) classifiers are trained and their individual results are then combined through a voting process. It is expected that RF performs more accurately and robustly than an individual DT classifier. Each tree contributes by giving a unit vote for the most frequent class to the input vector \mathbf{x} and the classification label is allocated to the input vector through a majority vote: $\hat{C}_{RF} = \text{majority vote } \{\hat{C}_t(\mathbf{x})\}_1^T$, where \mathbf{x} is the input vector, $\hat{C}_t(\mathbf{x})$ is the class prediction of the t th tree, and T shows the total number of trees [49], [50].

2) *Support Vector Machine (SVM)*: Exploiting the training data, SVM searches for a separating hyperplane (class boundary) with the largest margin [38]. To train the classifier and locate the hyperplane, only the samples that are close to the class boundaries are needed (i.e., support vectors). In other words, these are the training samples that influence the most in placing the hyperplane in the feature space. Because of this, SVM performs well when a limited number of training samples are available [37], [50], [51].

SVM was originally developed as a linear classifier to solve binary classification problems [52]. However, for classification problems, decision boundaries are often nonlinear. To tackle this, the linear SVM approach was extended for nonlinear separable cases by the so-called kernel methods. For this, the data are projected into a high-dimensional feature space where the samples are linearly separable. The final hyperplane decision function is

defined as

$$f(\mathbf{x}) = \left(\sum_{i=1}^n \alpha_i y_i \mathbf{K}(\mathbf{x}_i, \mathbf{x}) + b \right)$$

where $\mathbf{x}_i \in \mathbb{R}^d$, $i = 1, \dots, n$ is a set of n training samples with their corresponding class labels $y_i \in \{1, +1\}$, α_i denotes the Lagrange multipliers, \mathbf{K} denotes the kernel function, and b refers to the bias. SVM only requires the definition of the kernel function \mathbf{K} and the regularization parameter [50]. To implement SVM for a multiclass classification problem, several methods were proposed in the literature, the one-against-one and one-against-all strategies are the most well-known and simplify the separation of a multiclass problem into several binary classification problems. For a detailed review on the SVM technique, we refer readers to [52].

IV. EXPERIMENTAL RESULTS

A. Data Description

Five drill-core samples were used to test the performance of the proposed machine learning framework (see Fig. 8). These samples were selected from sections at different depths to guarantee the presence of slightly varying alteration patterns and mineral assemblages. In general, the matrix in the samples is dominantly composed of feldspars altered at different degrees to white mica. Disseminated chlorite and biotite are also found. The samples show veins of varying composition with white mica alteration halos of different thicknesses. This can be linked to the differences between the temperatures and the chemistry of the

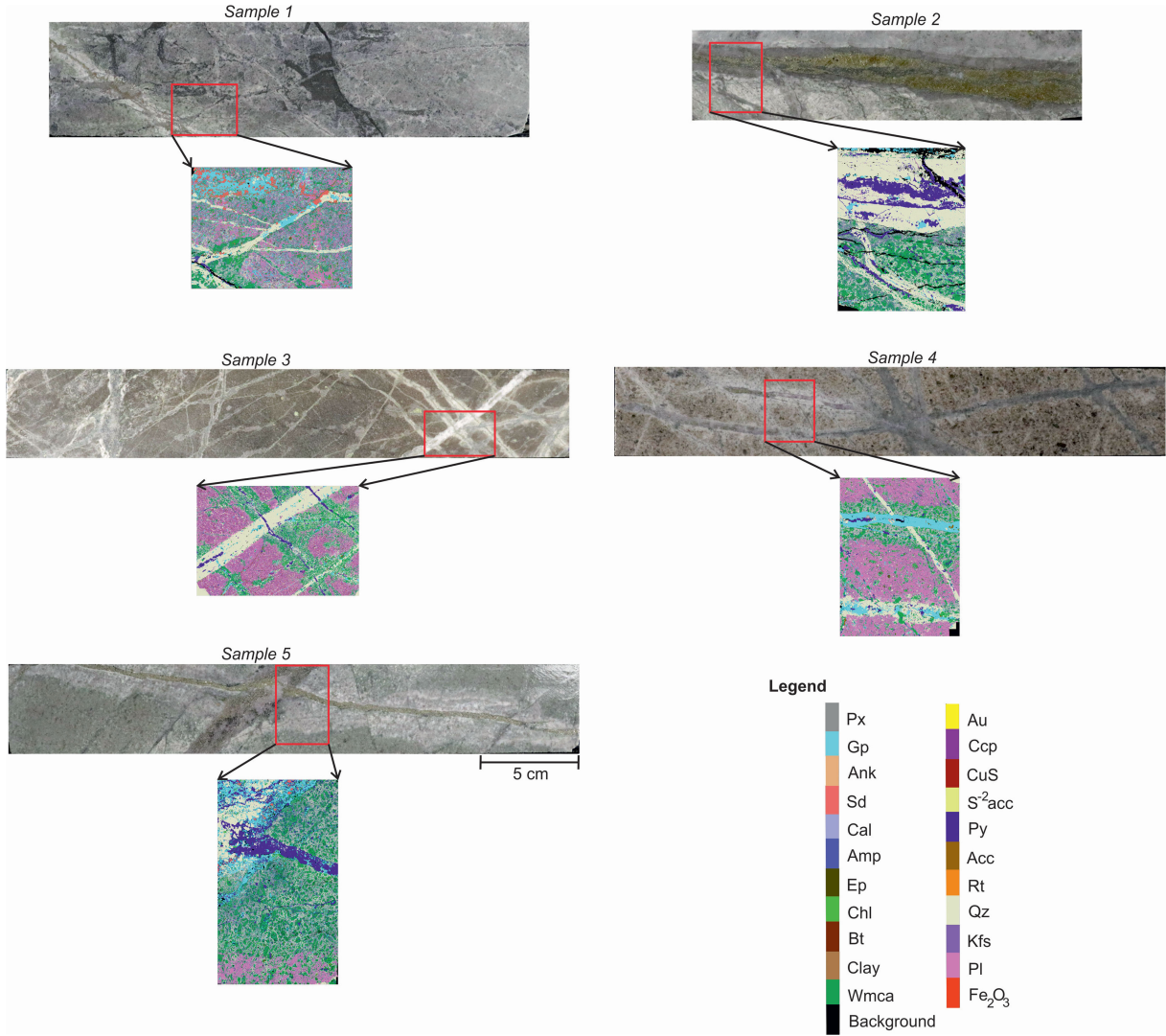


Fig. 8. RGB image of the drill-core samples used to test the proposed system. The area surrounded by red is where the thin sections for the SEM-MLA analysis were performed. The original MLA images, obtained from the SEM-MLA analysis, are shown below the drill-cores and are stretched for visualization. The pixel size in the original MLA images is about $3 \mu\text{m}$. Mineral abbreviations after [48].

mineralizing fluids. In *sample 1*, there are quartz-gypsum veins, thicker siderite-gypsum veins, and a fine pyrite vein. *Sample 2* shows a large vein composed by mostly pyrite with less gypsum. In *sample 3*, fine pyrite and quartz veins are presented. Very fine pyrite-gypsum veins and quartz veins are presented in *sample 4*. Finally, *sample 5* shows one thin pyrite vein which seems to be overprinted with a thicker pyrite-quartz-anhydrite vein.

These drill-cores were scanned to acquire their corresponding HS images. After performing SEM-MLA analysis on characteristic sections, the resultant MLA images were resampled from $3 \mu\text{m}/\text{pixel}$ to $1.5 \text{ mm}/\text{pixel}$, corresponding to the pixel size of the HS data. The labeling was based on the most dominant mineral in the MLA map within the pixel size of the HS data. From this, seven classes were obtained. However, classes with less than 10 pixels were discarded resulting in a total of five classes (see the upper-left image in Fig. 9). As explained in Section III, for these classes a soft labeling strategy was proposed. Thus, detailed abundance information for each of the

classes is provided along with the MLA resampled map (see the upper-right image in Fig. 9). As an example, *class 1* is rich in white mica with less quartz and feldspars; *class 2* has mainly gypsum; *class 3* is dominated by a nonactive VNIR-SWIR mineral (i.e., plagioclase) with a mixture of white mica, chlorite, and biotite as the active VNIR-SWIR minerals; *class 4* is also dominated by a nonactive VNIR-SWIR mineral, quartz, and white mica mixed with gypsum; finally, *class 5* is composed mainly of pyrite, a nonactive VNIR-SWIR mineral.

B. Experimental Setup

RF and SVM were used as the classifiers (see mineral maps at the bottom of Fig. 9). The number of trees is set to 500 for the RF. The number of prediction variables is set equal to the number of input bands. In the case of SVM, radial basis function (RBF) kernel is used. The optimal hyperplane parameters C (parameter that controls the amount of penalty during the SVM

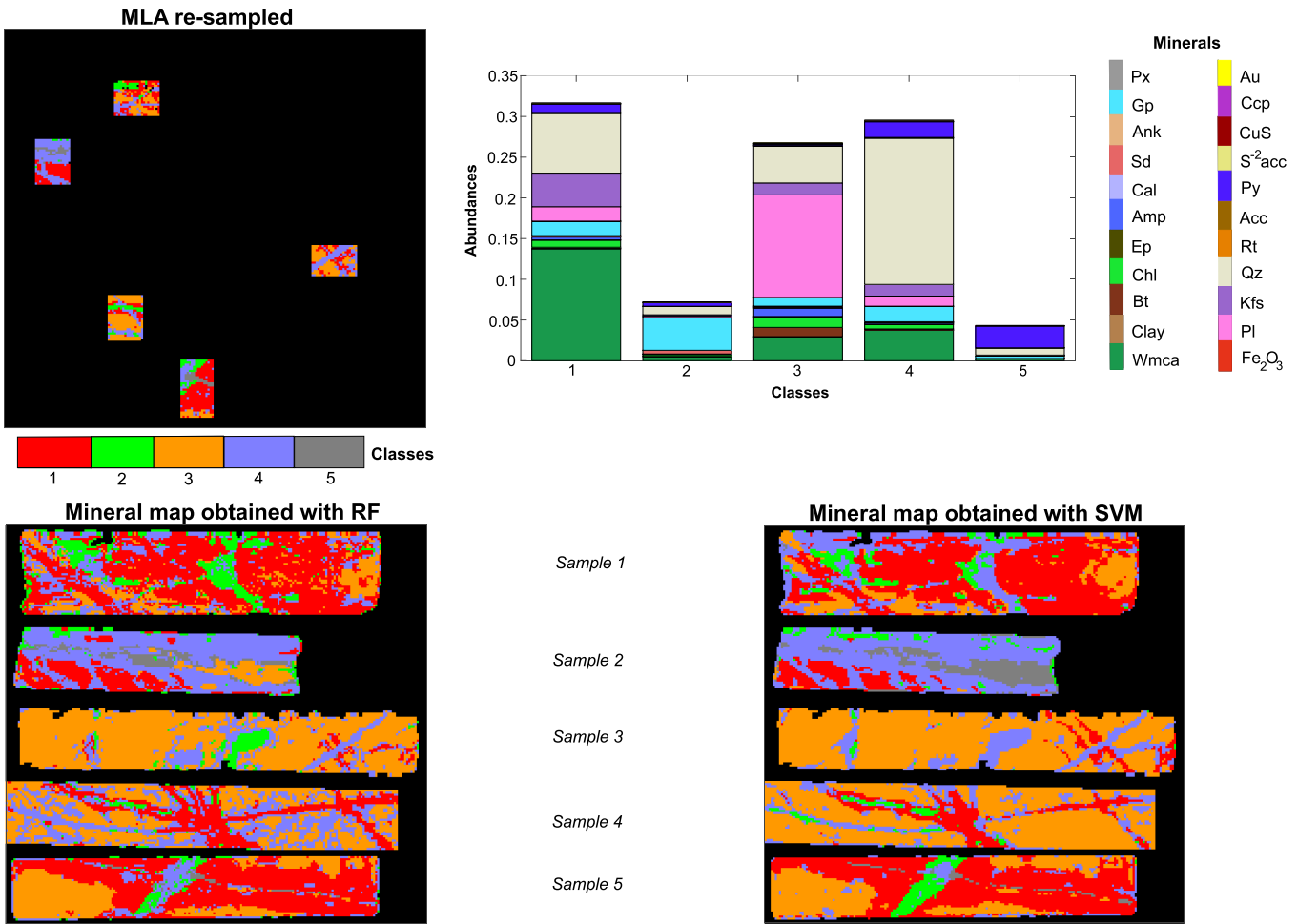


Fig. 9. Classification results obtained by selecting training samples from the mosaic of the MLA resampled images and using supervised classification algorithms: Random forest (RF) and support vector Machine (SVM). Mineralogical abundances in the resultant classes are given in the upper-right bar graph. Mineral abbreviations after [48].

TABLE IV
TOTAL NUMBER OF SAMPLES AVAILABLE IN THE REFERENCE DATA

Class	Total	Training	Test
1	601	480	121
2	141	112	29
3	509	407	102
4	554	443	111
5	83	66	17

optimization) and γ (spread of the RBF kernel) have been determined to $C = 4.4e + 03$ and $\gamma = 5.2e - 04$ using fivefold cross validation.

C. Quantitative and Qualitative Assessment

To quantitatively evaluate the performance of RF and SVM, we followed an 80-20 approach where 80% of the available reference samples were randomly selected as the training set and 20% as the test set (see Table IV). The experiment was repeated 30 times to avoid any bias and obtain a statistically sound result and the mean values for the accuracies are reported in Table V. The obtained low accuracy values were expected due to the mixed

TABLE V
OVERALL AND AVERAGE CLASSIFICATION ACCURACIES [%]

Accuracies	RF	SVM
Overall	69.6 (± 2.2)	73.9 (± 2.1)
Average	62.1 (± 3.1)	67.5 (± 2.9)

nature of the training samples. However, SVM outclassed RF by 4.3% and 5.4% for the overall and average accuracy, respectively. Moreover, based on the variability of the overall and average accuracies provided by the standard deviation, SVM produces slightly more stable results than RF.

Confusion matrices presented in Tables VI and VII (bold values represent the correctly classified samples) show that more samples have been missclassified with RF than with SVM. To illustrate, for RF, out of 29 available test samples in *class 2*, only 17 samples were correctly classified and from the 12 missclassified, half of them were wrongly classified as *class 4*. However, with SVM, 20 samples were correctly classified and from the nine missclassified samples only four samples are classified as *class 4*. From these tables, it is also possible to see how samples in *class 3* are being mostly missclassified as *class 4* by RF.

TABLE VI
CONFUSION MATRIX RF [SAMPLES]

		Predicted				
		1	2	3	4	5
Expected	1	86	8	16	10	1
	2	1	17	2	6	3
	3	10	0	76	16	0
	4	15	3	14	77	2
	5	2	1	0	7	7

TABLE VII
CONFUSION MATRIX SVM [SAMPLES]

		Predicted				
		1	2	3	4	5
Expected	1	96	1	15	9	0
	2	4	20	0	4	1
	3	9	0	85	8	0
	4	16	2	13	80	0
	5	2	1	0	9	5

The missclassification is understandable since the labels for the classes are based on a degree of membership where the same minerals are presented in all classes but their abundances differ. This means that we are mapping mixtures of minerals instead of pure minerals.

For the qualitative analysis, the resultant mineral maps are shown in Fig. 9. In general, the majority of the structural features and mineral distributions present in the surface of the drill-core samples are well characterized. For example, in *sample 4*, the structure of the veins is correctly mapped and differences in the mineralogical composition along the veins are also mapped. To illustrate, the vein varies from a purer muscovite content (*class 1*) on the right side and middle part of the vein to a more muscovite-gypsum rich vein with higher amounts of nonactive VNIR-SWIR minerals (*class 4*) on the left side of the vein. The variations in the spectra within these two classes are mainly in the intensity of the reflectance. As another example, an alteration in the middle of *sample 3*, which is not actually visible in the red-green-blue (RGB) image of the sample (see Fig. 8), is being mapped. This highlights the capabilities of HS data to uncover alteration patterns that are not visible to the human eye. However, in this central area, there are differences in the classes assigned by RF and SVM. With RF this area is being mapped as *class 2* and with SVM as *class 4*. Another example of this occurs in *sample 1*, where the vein in the central area has been classified as *class 2* with RF, whereas with SVM, it corresponds mainly to *class 4*. Similarly, in *sample 2*, the central vein composed of pyrite has been correctly classified as *class 5* with SVM. However, with RF this vein is being mapped as *class 3* which is rich in feldspars (nonactive VNIR-SWIR minerals as pyrite) but also muscovite, biotite, and chlorite. Regarding the upper gypsum vein in this sample, in any of the two maps this vein has been completely mapped, but only a very thin area of it. All these differences in the mapped classes can be linked to the confusion matrices. To illustrate, the matrix in *sample 4* is being classified as a *class 3* and *class 4* by RF and mostly as *class 3* with SVM. However, from the confusion matrices it is possible to see that the majority of the missclassified samples in *class 3*

with RF are assigned to *class 4*, whereas with SVM the number of missclassified samples for *class 3* is lower.

To complement the visual analysis of these results, two mineral maps were obtained by using SAM (see Fig. 10). The end-members utilized for the first map (v1) were derived by using PPI and n-D visualizer implemented in the ENVI software. From this, six classes were found and the same number of endmembers was used when implementing VCA to extract the second set of endmembers for the mineral map v2. These endmembers were labeled by comparing them with a reference spectral library. Fig. 10 shows the extracted endmembers and corresponding interpreted labels. From this, it can be seen that the main minerals are white mica, gypsum, chlorite, and biotite, which also correspond to the most abundant VNIR-SWIR active minerals mapped in the MLA resampled image. To generate the mineral maps, SAM was used on specific regions of the electromagnetic spectrum that encompass the diagnostic absorption features of each of the main minerals (Wmca, Gp, Chl-Bt). These ranges were 1289–1659 nm, 1848–1948 nm, and 2136–2278 nm. After some trials, a minimum angle of 0.05 was selected for a better mapping. In general, although the same angle was used for both maps, there is a higher number of unclassified pixels in v2. Nonetheless, both maps show the main structural patterns of all the samples, except for *sample 1*, where the central alteration has been slightly delineated and the left vein has been only mapped in v1. Differences in the classification of the *Chl + Wmca* endmember are especially seen in the matrix of *sample 4* and *sample 5*, which can be attributed to the higher content of Wmca in the PPI endmember. Another relevant difference is observed for *sample 4*, where a better mapping was achieved using the endmembers obtained by VCA.

Finally, to complete the examination of the capabilities of our proposed method, we looked at the center spectra from the training samples and the test samples (see Fig. 11). The center spectrum is the sample spectrum closest to the mean. From these plots, it can be seen that the general shape of the training center spectra fit the general shape of their respective center spectra in the test sets. The main absorption features present in the center spectra from the training samples are also found in the center spectra from the test samples, as for example in *class 1*. However, with SVM, this is not that obvious and the center spectra from the test set are more influenced by the nonactive VNIR-SWIR minerals which results in a low-intensity reflectance spectrum trend. Also, for *class 3*, which based on the soft labeling, it is dominated by nonactive VNIR-SWIR minerals with a mixture of white mica, chlorite, and biotite, as the active VNIR-SWIR minerals, the center spectrum for the training samples shows the higher content of white mica. However, the center spectra for the test samples, in both RF and SVM, are dominated by chlorite-biotite with less gypsum and muscovite.

V. DISCUSSION

In this paper, we propose a framework to map minerals in drill-cores using a fusion of VNIR-SWIR HS data and high-resolution mineralogical analysis. High-resolution mineralogical information is used as reference data to train a supervised classifier to up-scale the detailed information coming from the

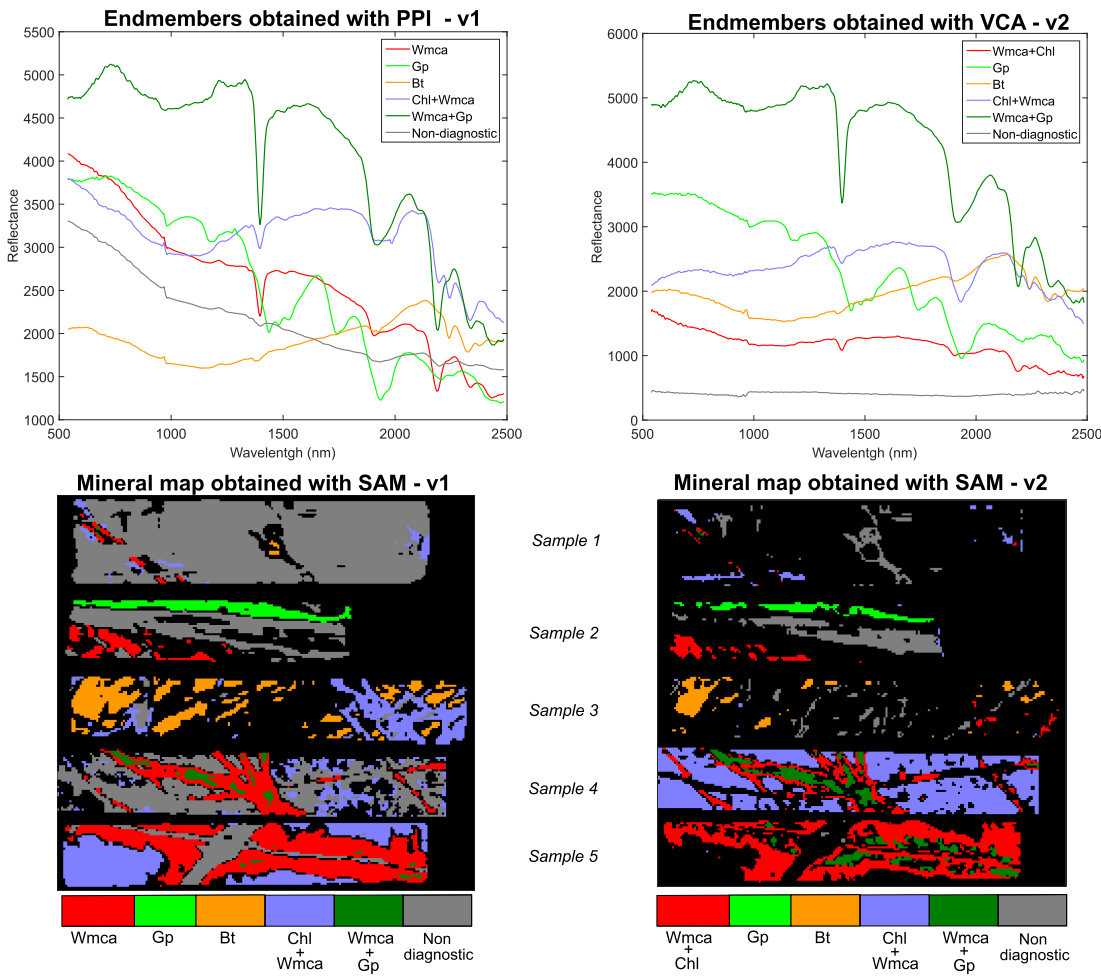


Fig. 10. Mineral maps obtained by the SAM on specific wavelength ranges that encompass the unique features of the endmembers. The extreme spectral responses, considered as the endmembers, were derived by using the chain of PPI and n-D Visualizer for v1 and by using VCA, for v2. The nondiagnostic endmember represents K-feldspars, silicates, or sulfates, amongst other VNIR-SWIR nonactive minerals. Mineral abbreviations after [48].

mineralogical analysis to entire drill-cores. For the mineralogical data, we suggested to use SEM-MLA since this is an imaging system which provides a complete model mineralogy allowing a better fusion with the HS images. However, it is important to highlight that the present approach is not restricted to the use of SEM-MLA analysis as reference data, but any other imaging method providing quantitative mineralogical data can be used as substitution of the MLA images.

To process the HS data and test the proposed approach, we organized the drill-core samples in a mosaic. This gives us the advantage of having more training samples per class than using the samples individually, which can be illustrated with *sample 5*. In this sample, only a few training samples for *class 3*, which corresponds to the matrix, are available in its corresponding MLA image. However, thanks to the mosaic, *class 3* is well mapped in the entire sample. As an additional added value, this mosaic brings us closer to the real situation in the mineral exploration industry, where high-resolution mineralogical analyses are performed only for small areas in certain segments of the entire drill-core. This allows the use of these areas to map minerals within their corresponding alteration zones where mineralogical assemblages tend to be similar. However, it is important to

clarify that for this study only five samples reaching a few more than 1 m were used while during exploration campaigns cores can take up to a few kilometers. Thus, all the areas selected for the SEM-MLA analysis must ideally be representative of all the alterations occurring in the drill-hole interval.

MLA and HS images are acquired at different spatial resolutions. To be able to fuse both data sets and develop a reference map out of the MLA image, we proposed a system to resample the MLA images. This starts by selecting the most dominant mineral in the MLA image for a HS pixel size, which in this study resulted in five classes. Then, to account for the fact that the SEM-MLA analysis detects more than just VNIR-SWIR active minerals we proposed a soft labeling strategy. Here, labels for each pixel are accompanied by a bar graph where information regarding the membership of the specific underlying minerals is provided. Hence, the relative abundance of all the minerals existing in the samples is available. From the results, we have seen the value of this labeling strategy which helped us to better understand the spectral changes amongst the classes in the mineral maps. Moreover, this is highly relevant to understand the mineral composition and associations within a mineralized system, which is essential in the evaluation of the distribution of target

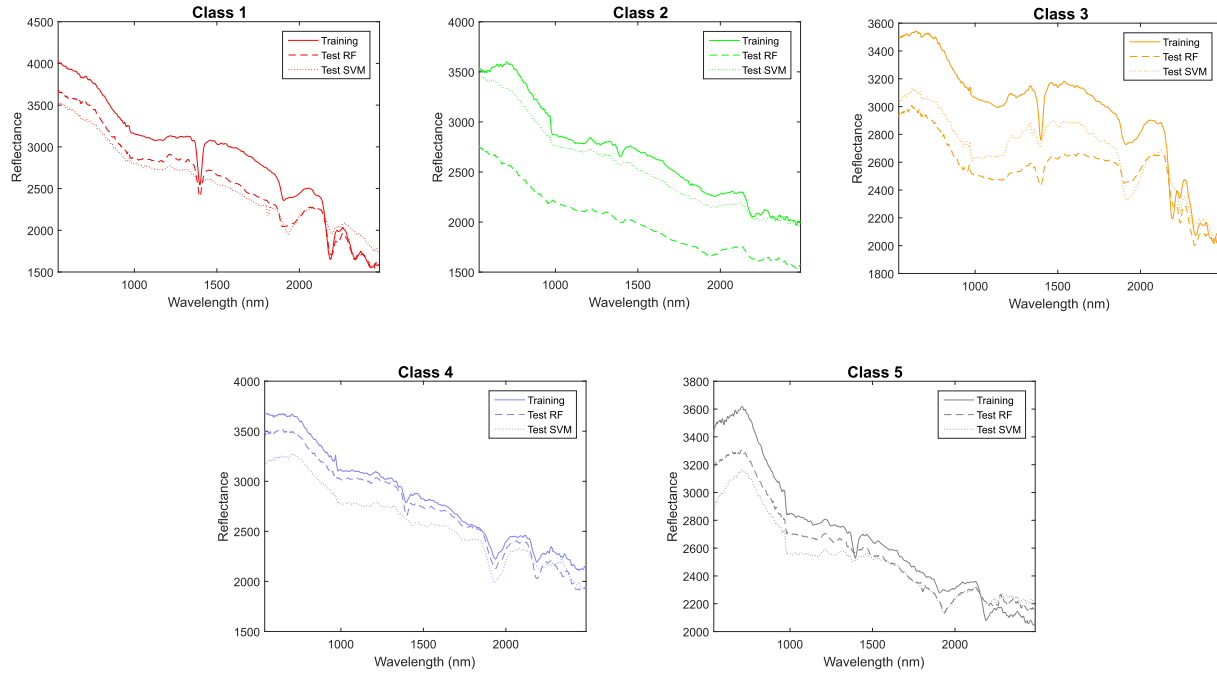


Fig. 11. Training and test center spectra from mineral maps obtained by RF and SVM.

commodities and the economical potential of the deposit. After resampling the MLA images, we coregistered both HS and MLA images by a visual analysis. However, this step could be automated by marking the desired areas for the mineralogical analysis before the acquisition of the HS data. This makes possible to find the specific coordinates of the MLA images in the HS data by automatic approaches. Another important fact regarding the SEM-MLA analysis is the selection for the areas where this analysis is performed. We have seen with *sample 2* how the upper gypsum vein is not well mapped in any of the resultant maps (RF and SVM maps). This is due to its corresponding MLA image, which is not representative enough of the entire sample. For this reason, special care needs to be taken for selecting the areas where the high-resolution mineralogical analysis are performed.

As the supervised classifiers, we tested two well-known algorithms, RF and SVM. From the resultant mineral maps, we have seen that both methods provide good results with slight differences in certain classes which might be attributed to the content of nondiagnostic minerals in the VNIR-SWIR range. Based on the accuracies and confusion matrices, SVM performs, to a certain extent, better than RF, especially when it comes to *class 1* and *class 3*. However, these are minor differences and together with the center spectra, it shows the suitability of the proposed framework to extrapolate and up-scale information from high-resolution mineralogical analysis of a small area to larger sections of drill-cores. In general, the proposed method offers an objective approach completely based on ground truth data up-scaled from high-resolution mineralogical analysis capable of achieving representative and descriptive mineral maps.

Finally, to illustrate the analysis that can be achieved by commonly used and available tools we implemented SAM in a specific wavelength range that enclose the main absorption features

of the endmembers. For the determination of the endmembers, two different approaches were used. The first map, obtained by endmembers derived from the chain of PPI and n-D visualizer, provided good results for a general characterization. For the second map, endmembers derived by the VCA algorithm were used and although the number of unclassified pixels is higher than in the first map, a slightly more detailed mapping was achieved. The experimental results obtained by these techniques indicate that the proposed method could be considered as a precise alternative approach for drill-core mineral mapping with minimal expert intervention. Note that the examined endmember extraction-based approaches imply the need of mineral spectroscopy knowledge and consist of several steps (e.g., determination of the number of endmembers), which may lead to major errors. Additionally, with our proposed approach the mineralogical understating of each class is possible, showing, for example, the influence of VNIR-SWIR featureless minerals in each of the classes and the relation with the general spectral shape. Also, the available quantitative mineralogical information helps with the interpretation of the endmembers which can be difficult due to the nonlinear relation between absorption features and mineral content, especially with mixed pixels.

VI. CONCLUSION

In this paper, we presented a supervised machine learning classification system for drill-core mineral mapping by fusing high-resolution mineralogical analysis and HS data. We suggested to use scanning electron microscopy (SEM)-based mineral liberation analysis (MLA) since it provides high resolution images useful to up-scale detailed mineralogical information to entire drill-core samples. We used the MLA image as reference

data to classify the drill-core HS image. We proposed a technique to resample the MLA image to the HS spatial resolution and coregister it to the HS image. Here, our proposed approach includes a soft labeling strategy where not only a single mineral describes a class but also a set of mineral memberships representative of the entire MLA images. Then, we exploited this detailed mineralogical information in the resampled MLA image by generating the training set and applying two well-known supervised machine learning classifiers, random forest and support vector machine.

After analyzing the results of the experiments carried out, we conclude that our suggested framework is effective for fusing high-resolution mineralogical information with HS data providing accurate quantitative and qualitative results. It allows up-scaling and spreading detailed mineralogical information coming from small portions of the drill-cores to entire drill-core samples. Hence, not only alteration patterns, such as veins, are possible to be mapped but also the mineralogical variations within them. With the proposed method and soft labeling strategy detailed maps are achieved and the relative abundance information of all the minerals presented in the sample is given. Moreover, even when using only VNIR-SWIR HS data, an estimation of the mapping of nonactive VNIR-SWIR minerals is possible by means of the SEM-MLA. In general, this paper presents a new effective and objective framework to map minerals in drill-core samples based on ground truth data by fusing two techniques used in the industry, which up until now have been commonly used independently.

In future developments, we will continue analyzing different possibilities to exploit the fusion of high-resolution mineralogical analysis with HS data to map minerals in drill-core samples. This includes different resampling and coregistration techniques as well as the use of different quantitative mineralogical methods.

ACKNOWLEDGMENT

The authors would like to thank Robert Zimmermann and Benjamin Melzer for the support with the acquisition of the hyperspectral data and Sandra Lorenz for the initial support. Sabine Gilbricht and Kai Bachmann are gratefully thanked for the support with the SEM-MLA analysis. The Associate Editor is thanked for handling the manuscript and the two anonymous reviewers for their constructive comments which have improved the manuscript.

REFERENCES

- [1] S. Gandhi and B. Sarkar, "Drilling," in *Essentials of Mineral Exploration and Evaluation*. New York, NY, USA: Elsevier, 2016, ch. 8, pp. 199–234.
- [2] G. Krahenbuhl, P. Hapugoda, K. Warren, and G. O'Brien, "A new method for obtaining detailed mineral information on individual coal particles at the size that they are used in coke making," in *Proc. Bowen Basin Symp.*, Oct. 2015, pp. 35–40.
- [3] N. Fox, A. Parbhakar-Fox, J. Moltzen, S. Feig, K. Goemann, and J. Huntington, "Applications of hyperspectral mineralogy for geoenvironmental characterization," *Minerals Eng.*, vol. 107, pp. 63–77, 2017.
- [4] W. Nikonow and D. Rammlmair, "Automated mineralogy based on micro-energy-dispersive X-ray fluorescence microscopy (μ -EDXRF) applied to plutonic rock thin sections in comparison to a mineral liberation analyzer," *Geoscientific Instrum., Methods Data Syst.*, vol. 6, no. 2, pp. 429–437, 2017.
- [5] R. Fandrich, Y. Gu, D. Burrows, and K. Moeller, "Modern SEM-based mineral liberation analysis," *Int. J. Mineral Process.*, vol. 84, no. 1–4, pp. 310–320, 2007.
- [6] P. Gottlieb *et al.*, "Using quantitative electron microscopy for process mineralogy applications," *JOM: J. Minerals, Metals Mater. Soc.*, vol. 52, no. 4, pp. 24–25, 2000.
- [7] E. Littlefield, W. Calvin, P. Stelling, and T. Kent, "Reflectance spectroscopy as a drill core logging technique: An example using core from the Akutan geothermal exploration project," *Geotherm. Res. Council Trans.*, vol. 36, pp. 1283–1291, 2012.
- [8] W. M. Calvin and E. L. Pace, "Mapping alteration in geothermal drill core using a field portable spectroradiometer," *Geothermics*, vol. 61, pp. 12–23, 2016.
- [9] F. A. Kruse, "Identification and mapping of minerals in drill core using hyperspectral image analysis of infrared reflectance spectra," *Int. J. Remote Sens.*, vol. 17, no. 9, pp. 1623–1632, 1996.
- [10] G. S. Taylor, "Mineral and lithology mapping of drill core pulps using visible and infrared spectrometry," *Natural Resour. Res.*, vol. 9, no. 4, pp. 257–268, 2000.
- [11] G. Bonifazi, N. Picone, and S. Serranti, "Ore minerals textural characterization by hyperspectral imaging," in *Proc. Image Process.: Algorithms Syst. XI. Proc. SPIE- IS&T Electron. Imag.*, SPIE, vol. 8655, 2013, Art. no. 865510.
- [12] R. N. Clark, "Spectroscopy of rocks and minerals, and principles of spectroscopy," in *Remote Sensing for the Earth Sciences: Manual of Remote Sensing*, vol. 3. New York, NY, USA: Wiley, 1999, ch. 1, pp. 3–58.
- [13] F. van der Meer, "Analysis of spectral absorption features in hyperspectral imagery," *Int. J. Appl. Earth Observ. Geoinformation*, vol. 5, no. 1, pp. 55–68, 2004.
- [14] P. R. Christensen *et al.*, "A thermal emission spectral library of rock-forming minerals," *J. Geophysical Res.: Planets*, vol. 105, no. E4, pp. 9735–9739, 2000.
- [15] R. F. Kokaly *et al.*, "USGS Spectral Library Version 7: U.S. Geological Survey Data Series 1035," Reston, VA, USA. [Online]. Available: <https://crustal.usgs.gov/speclab/QueryAll07a.php>
- [16] J. F. Huntington *et al.*, "Automated mineralogical core logging at the Emmie Bluff iron oxide-copper-gold prospect," *Mesa J.*, vol. 41, pp. 38–44, Apr. 2006.
- [17] A. J. Mauger and S. Hore, "Integrating mineralogical interpretation of HyLogger data with HyMap mineral mapping, Mount Painter, South Australia," in *Innovations in Remote Sensing and Photogrammetry, Lecture Notes in Geoinformation and Cartography*. Berlin, Heidelberg, Germany: Springer, 2009, pp. 271–280.
- [18] A. J. Mauger, J. L. Keeling, and J. F. Huntington, "Alteration mapping of the Tarcoola Goldfield (South Australia) using a suite of hyperspectral methods," *Appl. Earth Sci.*, vol. 116, no. 1, pp. 2–12, 2007.
- [19] E. F. Littlefield and W. M. Calvin, "Geothermal exploration using imaging spectrometer data over Fish Lake Valley, Nevada," *Remote Sens. Environ.*, vol. 140, pp. 509–518, 2014.
- [20] F. A. Kruse, R. L. Bedell, J. V. Taranik, W. A. Peppin, O. Weatherbee, and W. M. Calvin, "Mapping alteration minerals at prospect, outcrop and drill core scales using imaging spectrometry," *Int. J. Remote Sens.*, vol. 33, no. 6, pp. 1780–1798, 2012.
- [21] N. Xu, Y.-X. Hu, B. Lei, Y.-T. Hong, and F.-X. Dang, "Mineral information extraction for hyperspectral image based on modified spectral feature fitting algorithm," *Spectrosc. Spectral Anal.*, vol. 31, no. 6, pp. 1639–1643, Jun. 2011.
- [22] E. Bedini, F. van der Meer, and F. van Ruitenbeek, "Use of HyMap imaging spectrometer data to map mineralogy in the Rodalquilar caldera, southeast Spain," *Int. J. Remote Sens.*, vol. 30, no. 2, pp. 327–348, 2009.
- [23] C. Kratt, W. M. Calvin, and M. F. Coolbaugh, "Mineral mapping in the Pyramid Lake basin: Hydrothermal alteration, chemical precipitates, and geothermal energy potential," *Remote Sens. Environ.*, vol. 114, no. 10, pp. 2297–2304, 2010.
- [24] T. J. Roache *et al.*, "Epidote-clinozoisite as a hyperspectral tool in exploration for Archean gold," *Australian J. Earth Sci.*, vol. 58, no. 7, pp. 813–822, 2011.
- [25] M. Mathieu, R. Roy, P. Launeau, M. Cathelineau, and D. Quirt, "Alteration Mapping on drill cores using a HySpex SWIR-320m hyperspectral camera: Application to the exploration of an unconformity-related uranium deposit (Saskatchewan, Canada)," *J. Geochemical Exploration*, vol. 172, pp. 71–88, 2017.
- [26] M. Tappert, B. Rivard, D. Giles, R. Tappert, and A. Mauger, "Automated drill core logging using visible and near-infrared reflectance spectroscopy: A case study from the Olympic Dam IOCG deposit, South Australia," *Econ. Geology*, vol. 106, no. 2, pp. 289–296, 2011.

- [27] W. Sun, J. Ma, G. Yang, B. Du, and L. Zhang, "A Poisson nonnegative matrix factorization method with parameter subspace clustering constraint for endmember extraction in hyperspectral imagery," *ISPRS J. Photogrammetry Remote Sens.*, vol. 128, pp. 27–39, 2017.
- [28] V. Rodriguez-Galiano, M. Sanchez-Castillo, M. Chica-Olmo, and M. Chica-Rivas, "Machine learning predictive models for mineral prospectivity: An evaluation of neural networks, random forest, regression trees and support vector machines," *Ore Geol. Rev.*, vol. 71, pp. 804–818, 2015.
- [29] R. J. Murphy, S. T. Monteiro, and S. Schneider, "Evaluating classification techniques for mapping vertical geology using field-based hyperspectral sensors," *IEEE Trans. Geosci. Remote Sens.*, vol. 50, no. 8, pp. 3066–3080, Feb. 2012.
- [30] V. Kuosmanen, H. Arkimaa, M. Tiainen, and R. Bärs, "Hyperspectral close-range LWIR imaging spectrometry—3 case studies," *Geophysical Signatures of Mineral Deposit Types in Finland*, Geological Survey of Finland, Special Paper 58, Espoo, Finland, pp. 117–144, 2015.
- [31] A. Parbhaker-Fox, B. Lottermoser, and D. J. Bradshaw, "Cost-Effective means for identifying acid rock drainage risks: Integration of the geochemistry-mineralogy-texture approach and geometallurgical techniques," in *Proc. 2nd Australasian Inst. Mining Metall. (AusIMM) Int. Geometallurgy Conf.*, 2013, pp. 143–154.
- [32] K. Laakso, M. Middleton, T. Heinig, R. Bärs, and P. Lintinen, "Assessing the ability to combine hyperspectral imaging (HSI) data with mineral liberation analyzer (MLA) data to characterize phosphate rocks," *Int. J. Appl. Earth Observ. Geoinformation*, vol. 69, pp. 1–12, 2018.
- [33] H. Arkimaa, V. Kuosmanen, M. Tiainen, and B. Rainer, "Hyperspectral analysis of drill cores from the Kedononjankulma Cu-Au deposit," in *Proc. Current Res.: 2nd GTK Mineral Potential Workshop*, Kuopio, Finland: Geologian tutkimuskeskus, Tutkimusraportti 207, Geological Survey of Finland, Report of Investigation 207, May 2014, pp. 26–27.
- [34] P. Pinet *et al.*, "MGM deconvolution of complex mafic mineralogy rock slab spectra from visible-near infrared imaging spectroscopy: Implications for the characterization of the terrestrial oceanic and lunar crust," in *Proc. WHISPERS 8th Conf.*, 2016, pp. 1–4.
- [35] L. Breiman, "Random Forest," *Mach. Learn.*, vol. 45, no. 1, pp. 5–32, 2001.
- [36] Z. Zhou, *Ensemble Methods: Foundations and Algorithms*. Boca Raton, FL, USA: CRC Press, Taylor and Francis Group, 2012.
- [37] C. Cortes and V. Vapnik, "Support-Vector Networks," *Mach. Learn.*, vol. 20, pp. 273–297, 1995.
- [38] B. Schölkopf and A. J. Smola, *Learning with Kernels*. Cambridge, MA, USA: MIT Press, 2002.
- [39] J. W. Boardman, F. A. Kruse, and R. O. Green, "Mapping target signatures via partial unmixing of AVIRIS data," *JPL TRS*, no. 23, pp. 23–26, 1995.
- [40] J. M. P. Nascimento and J. M. B. Dias, "Vertex component analysis: A fast algorithm to unmix hyperspectral data," *IEEE Trans. Geosci. Remote Sens.*, vol. 43, no. 4, pp. 898–910, Apr. 2005.
- [41] S. Jakob, R. Zimmermann, and R. Gloaguen, "The need for accurate geometric and radiometric corrections of drone-borne hyperspectral data for mineral exploration: MEPhySTo—A toolbox for pre-processing drone-borne hyperspectral data," *Remote Sens.*, vol. 9, no. 1, 2017, Art no. 88.
- [42] A. Savitzky and M. Golay, "Smoothing and differentiation of data by simplified least squares procedures," *Anal. Chem.*, vol. 36, no. 8, pp. 1627–1639, 1964.
- [43] Y. Gu, "Automated scanning electron microscope based mineral liberation analysis an introduction to JKMR/FEI mineral liberation analyser," *J. Minerals Mater. Characterization Eng.*, vol. 02, no. 01, pp. 33–41, 2003.
- [44] H. Pattee, V. Cosslett, and A. Engström, *X-ray Optics and X-ray Microanalysis*. Cambridge, MA, USA: Academic Press, 1963.
- [45] P. J. Sylvester, "Use of the mineral liberation analyzer (MLA) for mineralogical studies of sediments and sedimentary rocks," *Mineralogical Assoc. Canada Short Course 42*, pp. 1–16, 2012.
- [46] K. Bachmann, M. Frenzel, J. Krause, and J. Gutzmer, "Advanced identification and quantification of in-bearing minerals by scanning electron microscope-based image analysis," *Microsc. Microanalysis*, vol. 23, no. 3, pp. 527–537, 2017.
- [47] M. Kern, R. Möckel, J. Krause, J. Teichmann, and J. Gutzmer, "Calculating the deportment of a fine-grained and compositionally complex Sn skarn with a modified approach for automated mineralogy," *Minerals Eng.*, vol. 116, pp. 213–225, 2018.
- [48] D. L. Whitney and B. W. Evans, "Abbreviations for names of rock-forming minerals," *Amer. Mineralogist*, vol. 95, no. 1, pp. 185–187, 2010.
- [49] V. F. Rodriguez-Galiano, B. Ghimire, J. Rogan, M. Chica-Olmo, and J. P. Rigol-Sánchez, "An assessment of the effectiveness of a random forest classifier for land-cover classification," *ISPRS J. Photogrammetry Remote Sens.*, vol. 67, no. 1, pp. 93–104, 2012.
- [50] P. Ghamisi, J. Plaza, Y. Chen, J. Li, and A. J. Plaza, "Advanced spectral classifiers for hyperspectral images: A review," *IEEE Geosci. Remote Sens. Mag.*, vol. 5, no. 1, pp. 8–32, Mar. 2017.
- [51] V. N. Vapnik, "An overview of statistical learning theory," *IEEE Trans. Neural Netw.*, vol. 10, no. 5, pp. 988–999, Sep. 1999.
- [52] B. Waske, J. A. Benediktsson, K. Arnason, and J. Sveinsson, "Mapping of hyperspectral AVIRIS data using machine-learning algorithms," *Can. J. Remote Sens.*, vol. 35, pp. S106–S116, 2009.



Isabel Cecilia Contreras Acosta received the B.Sc. (Hons.) degree in geological engineering from the University of Los Andes in Mérida, Venezuela in 2013, and the M.Sc. degree in geo-information science and earth observation for applied earth science with a specialization in natural hazards, risk, and engineering in 2017 from the ITC Faculty, University of Twente, The Netherlands. Since 2017, she is working toward Ph.D. degree in the machine learning group within the Exploration Department at the Helmholtz Institute Freiberg for Resource Technology - Helmholtz-Zentrum Dresden-Rossendorf (HZDR), Freiberg, Germany. Her research focuses on machine learning techniques for hyperspectral data analysis applied to mineral exploration.



Mahdi Khodadadzadeh received the B.S. degree in electrical engineering, electronics from the Sadjad University of Technology, Mashhad, Iran, in 2008 and the M.Sc. degree in electrical engineering, communications, from Tarbiat Modares University, Tehran, Iran, in 2011. In 2015, he received the Ph.D. degree from the Department of Technology of Computers and Communications, Escuela Politécnica, University of Extremadura, Cáceres, Spain, under the joint supervision of Prof. Antonio Plaza and Prof. Jun Li.

From 2015 to 2017, he was a Postdoctoral Researcher with the Remote Sensing Laboratory, Department of Information Engineering and Computer Science, University of Trento, Italy. Since 2017, he has worked as a Machine Learning Specialist with the Exploration Technology Division, Helmholtz Institute Freiberg for Resource Technology, Freiberg, Germany, where he is leading the machine learning group activities on hyperspectral drill core data analysis. His research interests include machine learning and image processing with application to remote sensing data analysis, and particular emphasis on hyperspectral data classification.

He has been a manuscript reviewer for the IEEE TRANSACTIONS ON GEOSCIENCE AND REMOTE SENSING, IEEE JOURNAL OF SELECTED TOPICS IN APPLIED EARTH OBSERVATIONS AND REMOTE SENSING, and IEEE GEOSCIENCE AND REMOTE SENSING LETTERS.



Laura Tusa received the B.Ss. degree in geological engineering from Babes Bolyai University, Cluj-Napoca, Romania in 2014 and the M.Sc. degree in georesources engineering from the University of Liege, Liege, Belgium, University of Lorraine, France and Luleå University of Technology, Sweden, in 2016. She is currently working toward the Ph.D. degree with the Helmholtz Institute Freiberg for Resource Technology, HZDR, and Freiberg Technical University, Freiberg, Germany. Her research focuses on the use of hyperspectral data in the framework of mineral exploration and mining.



Pedram Ghamisi (S'12–M'15–SM'18) received the B.Sc. degree in civil (survey) engineering from the Tehran South Campus of Azad University, Tehran, Iran, in 2008, the M.Sc. degree (Hons.) in remote sensing from the K. N. Toosi University of Technology, Tehran, Iran, in 2012, and the Ph.D. degree in electrical and computer engineering from the University of Iceland, Reykjavik, Iceland, in 2015.

In 2013 and 2014, he was with the School of Geography, Planning and Environmental Management, University of Queensland, Brisbane, QLD, Australia. In 2015, he was a Postdoctoral Research Fellow with the Technical University of Munich (TUM), Munich, Germany, and Heidelberg University, Heidelberg, Germany. From 2015 to 2018, he was a Research Scientist with the German Aerospace Center (DLR), Oberpfaffenhofen, Germany. Since 2018, he has been working as the Head of the Machine Learning Group, Helmholtz-Zentrum Dresden-Rossendorf (HZDR), Freiberg, Germany. He is also the CTO and the Co-Founder of VasoGnosis Inc., Milwaukee, WI, USA, where he is involved in the development of advanced diagnostic and analysis tools for brain diseases using cloud computing and deep learning algorithms. His research interests include interdisciplinary research on remote sensing and machine (deep) learning, image and signal processing, and multisensor data fusion.

Dr. Ghamisi was a recipient of the Best Researcher Award for M.Sc. students at the K. N. Toosi University of Technology in the academic year of 2010–2011, the IEEE Mikio Takagi Prize for winning the Student Paper Competition at IEEE International Geoscience and Remote Sensing Symposium (IGARSS) in 2013, the Talented International Researcher by Iran's National Elites Foundation in 2016, the first prize of the data fusion contest organized by the Image Analysis and Data Fusion Technical Committee (IADF) of IEEE-GRSS in 2017, the Best Reviewer Prize of IEEE GEOSCIENCE AND REMOTE SENSING LETTERS (GRSL) in 2017, the Alexander von Humboldt Fellowship from the Technical University of Munich, and the High Potential Program Award from HZDR. He serves as an Associate Editor for *Remote Sensing* and IEEE GRSL.



Richard Gloaguen received the Ph.D. degree Doctor Communitatis Europae in marine geosciences from the University of Western Brittany, Brest, France, in collaboration with the Royal Holloway University of London, Egham, U.K., and Göttingen University, Göttingen, Germany, in 2000.

He was a Marie Curie Postdoctoral Research Associate at the Royal Holloway University of London from 2000 to 2003. He led the Remote Sensing Group at University Bergakademie Freiberg, Freiberg, Germany, from 2003 to 2013. Since 2013, he has been

leading the division Exploration Technology at the Helmholtz-Institute Freiberg for Resource Technology, Freiberg, Germany. He is currently involved in UAV-based multisource imaging, laser-induced fluorescence, and noninvasive exploration. His research interests focus on multisource and multiscale remote sensing integration.